

# Catalysis Science & Technology

Accepted Manuscript



This is an *Accepted Manuscript*, which has been through the RSC Publishing peer review process and has been accepted for publication.

*Accepted Manuscripts* are published online shortly after acceptance, which is prior to technical editing, formatting and proof reading. This free service from RSC Publishing allows authors to make their results available to the community, in citable form, before publication of the edited article. This *Accepted Manuscript* will be replaced by the edited and formatted *Advance Article* as soon as this is available.

To cite this manuscript please use its permanent Digital Object Identifier (DOI®), which is identical for all formats of publication.

More information about *Accepted Manuscripts* can be found in the [Information for Authors](#).

Please note that technical editing may introduce minor changes to the text and/or graphics contained in the manuscript submitted by the author(s) which may alter content, and that the standard [Terms & Conditions](#) and the [ethical guidelines](#) that apply to the journal are still applicable. In no event shall the RSC be held responsible for any errors or omissions in these *Accepted Manuscript* manuscripts or any consequences arising from the use of any information contained in them.

# One-pot synthesis of mesoporous ZrPW solid acid catalyst for liquid phase benzylation of anisole

Zhichao Miao<sup>a,b</sup>, Huanling Song<sup>a,c</sup>, Huahua Zhao<sup>a</sup>, Leilei Xu<sup>a,b</sup>, Lingjun Chou<sup>a,c\*</sup>

## Abstract

Mesoporous zirconium phosphotungstate (M-ZrPW), accompanying large specific surface area ( $\sim 170 \text{ m}^2 \cdot \text{g}^{-1}$ ), big pore volume ( $\sim 0.25 \text{ cm}^3 \cdot \text{g}^{-1}$ ), uniform pore size distribution ( $\sim 6.5 \text{ nm}$ ) and tunable W/Zr ratios (0-0.2), was successfully prepared via a facile one-pot evaporation-induced self-assembly (EISA) strategy. Small-angle X-ray diffraction (SAXRD), transmission electron microscopy (TEM) and scanning electron microscopy (SEM) characterizations showed that these materials had obvious mesoporous structure even when the W/Zr ratio reached up to 0.2. The tungsten species introduced via this strategy highly dispersed among the wall of mesoporous framework. More importantly, the tungsten species greatly improved the Brønsted acidic property and catalytic activity in the Friedel-Crafts benzylation reaction. The highest activity was obtained at a W/Zr ratio of 0.2 with the strongest Brønsted acidity. In addition, the influences of various reaction parameters such as reaction time, amount of catalyst and calcination temperature of catalyst, were detailedly investigated in this paper. Furthermore, the M-ZrPW showed higher catalytic activity than H-Beta, H-ZSM5 and ZrPW prepared by sol-gel method. Meanwhile, M-ZrPW could be reused at least for five cycles in the benzylation reaction without obvious decrease of catalytic activity.

**Keywords:** one-pot strategy, mesoporous ZrPW, excellent textural properties, high dispersion, Brønsted acid.

## 1. Introduction

Friedel-Crafts (FC) benzylation is one of the fundamental reactions in the field of organic synthesis for the preparation of fine chemicals, dielectric fluids and pharmaceutical chemicals.<sup>1-4</sup> Conventionally, FC benzylation reaction is catalyzed by strong homogeneous acid such as  $\text{AlCl}_3$ ,  $\text{FeCl}_3$ ,  $\text{ZnCl}_2$  and  $\text{H}_2\text{SO}_4$ .<sup>2,5</sup> Nevertheless, the complete separation of products from these reaction mixtures usually requires an expensive and tedious purification process. Therefore, from the viewpoint of green chemistry, the efficient solid acid catalysts should be developed since these are reusable, readily separable, environmentally friendly and can lead to minimal pollution and waste.<sup>6-8</sup> In addition, the FC benzylation reactions catalyzed by solid acid catalysts have been attracting considerable attention in recent years.<sup>9-11</sup> Many kinds of solid acid catalysts were utilized in these reactions, such as zeolites,<sup>12,13</sup> ion-exchanged resins,<sup>14,15</sup> sulfated metal oxide,<sup>16</sup> Ga-, Al-, GaAl-SBA-15,<sup>17</sup> niobium phosphate,<sup>18,19</sup> heteropoly acids and their salts.<sup>20-22</sup> Moreover, as for the benzylating agents, benzyl chloride and benzyl alcohol are commonly employed in the FC benzylation reactions.<sup>23,24</sup> Compared with benzyl chloride, which produces HCl, an environmental undesirable product, benzyl alcohol only generates water as a side product in the reaction, therefore, the use of benzyl alcohol instead of benzyl chloride is an eco-friendly process.<sup>25,26</sup>

Since the discovery of MCM-41,<sup>27,28</sup> a variety of mesoporous materials have been fabricated and widely applied in many fields, such as the separation,<sup>29</sup> sorption,<sup>30</sup> controlled release<sup>31</sup> and heterogeneous catalysis.<sup>32</sup> The solid acid catalyst with

mesostructure, allows the reactant molecules access additional active acid sites in the pores, resulting in improved catalytic activity.<sup>33,34</sup> Mesoporous Nb<sub>2</sub>O<sub>5</sub>, Ta-W, Nb-W and Nb-Mo oxides were successfully synthesized and used as solid acid catalyst in FC benzylation of anisole, and their activities were higher than many conventional solid acid catalysts.<sup>35-38</sup> Moreover, the sulfated mesoporous Nb and Ta oxides with large specific surface area were prepared and showed excellent activity in the acid catalytic reactions.<sup>39-41</sup> Recently, the mesoporous zirconium oxophosphate (M-ZrPO) materials had been successfully synthesized in our previous work and used as solid acid catalyst in the ketalization reaction.<sup>42</sup> On this basis, we suggest that the introduction of tungsten into the M-ZrPO materials may enhance their acidic property owing to the high oxidation states of tungsten.<sup>36,37</sup> Besides, as far as we know, the reports related with synthesis of mesoporous zirconium phosphotungstate (M-ZrPW) materials through one-step strategy are very few and have potential to be investigated.

In this paper, one-pot evaporation-induced self-assembly (EISA) strategy was employed to synthesize a series of M-ZrPW with different content of tungsten. The characterizations of small X-ray diffraction (SXRD), transmission electron microscopy (TEM), scanning electron microscopy (SEM) and N<sub>2</sub>-physisorption were employed to illustrate the mesostructure of materials. Moreover, UV-visible diffuse reflectance spectra (UV-vis), Fourier transform infrared (FT-IR) and X-ray photoelectron spectroscopy (XPS) characterizations were used to investigate the chemical bonds in the materials. In addition, the influences of highly dispersed tungsten species on Brønsted acidic property and catalytic activity of M-ZrPW in

benzylation reaction were discussed detailedly. Furthermore, the solid acid catalyst was reused for five cycles to investigate the reusability of M-ZrPW in the FC benzylation reaction.

## 2. Experimental Section

### 2.1 Synthesis of Mesoporous Zirconium Phosphotungstate.

(EO)<sub>106</sub>(PO)<sub>70</sub>(EO)<sub>106</sub> triblock copolymer (Pluronic F127,  $M_{av}$  = 12600, Sigma-Aldrich), zirconyl chloride octahydrate ( $ZrOCl_2 \cdot 8H_2O$ ,  $\geq 99.0\%$ , Tianjin Fengyue Reagent Company), trimethyl phosphate ( $PO(OCH_3)_3$ ,  $\geq 99.0\%$ , Sinopharm Chemical Reagent Co. Ltd.), ammonium tungsten ( $(NH_4)_5H_5[H_2(WO_4)_6] \cdot H_2O$ ,  $\geq 99.0\%$ , Sinopharm Chemical Reagent Co. Ltd.), ethanol ( $\geq 99.7\%$ , Sinopharm Chemical Reagent Co. Ltd.). All the reagents were A.R. grade and used as received without further purification.

Mesoporous zirconium phosphotungstate (M-ZrPW) was synthesized via an improved one-pot evaporation-induced self-assembly (EISA) strategy.<sup>43,44</sup> In a typical procedure of synthesizing M-ZrPW, 1.2 g of F127 was employed as structure-directing agents (SDAs) and dissolved in 15 ml of anhydrous ethanol. As the SDAs were completely dissolved, 5 mmol of  $ZrOCl_2 \cdot 8H_2O$ , 3.75 mmol of  $PO(OCH_3)_3$  (the molar ratio of P/Zr was 0.75) and 0-1 mmol of tungsten species were added into the above solution with vigorous stirring. The solution was covered with PE film and stirred for 6 h at least. Finally, the solution mixture was transferred to a petri dish (d=9 cm) to undergo the slow EISA process at 60 °C for 48 h, then 100 °C for 24 h in a

drying oven. The obtained xerogel was calcined by slowly increasing temperature (1 °C /min ramping rate) to 500 °C and kept at the final temperature for 6 h to remove the SDAs. The obtained template-free self-assembled M-ZrPW was denoted as M-ZrPW-X, where X (0, 5, 10, 15, 20, 25) stands for the molar percentage ratio of W/Zr and the detailed characterization and discussion about M-ZrPW-25 were shown in the supporting information. For comparison, the ZrPW synthesized from sol-gel method was as reported by Chudasama *et al*<sup>45</sup> and the molar ratios of Zr, P, W were kept consistent with the M-ZrPW-20.

## 2.2 Characterization.

Powder X-ray diffraction (XRD) measurements were performed using an X'Pert Pro Multipurpose diffractometer (PANalytical, Inc.) with Cu K $\alpha$  radiation (0.15406 nm) at room temperature from 0.6° to 5.0° (small angle) and 10.0° to 80.0° (wide angle). Measurements were conducted using a voltage of 40 kV, current setting of 20 mA for small angle XRD and 40 mA for wide angle XRD, step size of 0.02°, and count time of 4 s.

The Raman spectra were recorded on a Laboram 010 confocal Raman System (Horiba JobinYvon, France) equipped with 632 nm He-Ne laser.

Transmission electron microscopy (TEM) images, fast Fourier transform (FFT) patterns, selected area electron diffraction (SAED) and energy-dispersive X-ray spectroscopy (EDX) measurements were performed on the TECNAI G<sup>2</sup> F20 high-resolution transmission electron microscopy under a working voltage of 200 kV.

The scanning electron microscopy (SEM) images were obtained on Hitachi Cold

FE-SEM SU80X0 high-resolution scanning electron microscopy.

The nitrogen adsorption and desorption isotherms at  $-196\text{ }^{\circ}\text{C}$  were recorded on an Autosorb-iQ analyzer (Quantachrome Instruments U.S.). Prior to the tests, all the samples were pretreated at  $200\text{ }^{\circ}\text{C}$  for 2 h. The specific surface areas were calculated via the Brunauer-Emmett-Teller (BET) method in the relative pressure range of 0.05-0.3; the single-point pore volume was calculated from the adsorption isotherm at a relative pressure of 0.990; pore size distributions were calculated using adsorption branches of nitrogen adsorption-desorption isotherms by Barrett-Joyner-Halenda (BJH) method.

Thermogravimetric-differential scanning calorimetry (TG-DSC) measurements were carried out on a NETZSCH STA 449F3 thermogravimetric analyzer from room temperature to  $1000\text{ }^{\circ}\text{C}$  with the rate of  $10\text{ }^{\circ}\text{C}/\text{min}$  under the air atmosphere.

UV-visible diffuse reflectance spectra were recorded on a PE Lambda 650S in the range of 190-700 nm.

Fourier transform infrared (FT-IR) spectra were recorded on KBr pellets by a Nexus 870 infrared spectrometer with the wave number from  $4000$  to  $400\text{ cm}^{-1}$ .

X-ray photoelectron spectroscopy (XPS) analyses of the samples were performed on a Thermo Scientific ESCALAB250xi spectrometer. All binding energies were calibrated to the  $\text{C}_{1s}$  line ( $284.8\text{ eV}$ ).

X-Ray Fluorescence (XRF) spectrum analyzer was recorded on a Magix PW2403 (PANalytical, Inc.).

Temperature programmed desorption of ammonia ( $\text{NH}_3$ -TPD) was performed on a



Tianjin Xianquan TP5000. A typical experiment for the TPD measurement was as follows: the M-ZrPW (0.1 g) was pretreated at 400 °C for 2 h in the flowing He to remove any moisture and absorbed impurities. After cooling to 100 °C, 10 mol% NH<sub>3</sub>-He was introduced for 30 min. Physically absorbed NH<sub>3</sub> was then removed by desorbing in He at 100 °C for 60 min. The TPD experiment was then carried out by raising the temperature of the sample in a programmed manner (10 °C/min) to 900 °C. The same sample without introduction of NH<sub>3</sub> was used as blank control and no TCD singles were observed in the programmed process from 100 to 900 °C.

The infrared spectra of adsorbed pyridine (Pyridine-IR) were recorded on PE Frontier FT-IR spectrometer. The sample (~15 mg) was pressed into a pellet (~13 mm), evacuated under vacuum at 400 °C for 1 h, then cooled to room temperature and pyridine was introduced and adsorbed for 30 min. The sample was raised to a desired temperature and evacuated for 30 min, after which the spectrum was recorded. The blank experiments were operated under the same conditions and used as the background to insure the accuracy of the infrared spectra of adsorbed pyridine. The Brønsted and Lewis acidity was determined by the method proposed by Emeis.<sup>46</sup>

### 2.3 Catalytic Reaction.

**Benylation of Anisole.** Liquid phase Friedel–Crafts (FC) benzylation of anisole was performed in a three-necked round bottom flask coupled with a reflux condenser in a temperature controlled oil bath as reported by Antonelli *et al.*<sup>39</sup> In a typical run, 0.2 g of M-ZrPW was added to a mixture of anisole and benzyl alcohol (20 mL anisole + 2 mL benzyl alcohol) with dodecane (0.4 ml) used as an internal standard

for gas chromatography (GC) analysis. Nitrogen was introduced into the flask through one of the gas inlets. The reaction was carried out at 170 °C under reflux condition with vigorous stirring for 2 h. The conversion of benzyl alcohol and selectivity of products were monitored by a gas chromatography (GC) instrument (Agilent-7890A; equipped with a flame ionization detector (FID) and HP-5 column (30 m × 0.32 mm × 0.25 μm)). Gas chromatography-mass spectroscopy (GC-MS) instrument (5975c vl MSD with triple-axis detector, GC Agilent-7890A) was employed to identify the reaction products. After completion of the reaction, the catalyst was separated by centrifugation and activated at 400 °C for 3 h for regeneration.

### 3. Results and discussion

#### 3.1. Mesoporous Structure

The small angle X-ray diffraction (SAXRD) is an important technique for the characterization of mesoporous materials.<sup>47,48</sup> The SAXRD patterns of M-ZrPW with different W/Zr ratios are shown in Fig 1.(1). The M-ZrPW-0, M-ZrPW-5 and M-ZrPW-10 presented a distinct diffraction peak in the range of 0.9-1° and one weak diffraction peak around 1.9°, which could be indexed as (100) and (110) reflections of *p6mm* two-dimensional hexagonal structure. These diffraction peaks indicated the existence of long-range ordered mesopores in these three samples. However, further increase the W/Zr ratios to 0.15 and 0.2, the SAXRD pattern only displayed a single broad peak at about 0.93° rather than the conspicuous diffraction peaks. Compared with the above-mentioned three samples, which had ordered mesostructure, the

orderliness of pores became poorer in the M-ZrPW-15 and M-ZrPW-20. (For the M-ZrPW-25, there was no diffraction peak in the SXRD patterns, indicating the completely disappearance of ordered mesostructure. The detailed discussion about M-ZrPW-25 was shown in the supporting information.) In addition, the small angle reflection peaks shifted to lower  $2\theta$  region (from  $0.99^\circ$  to  $0.93^\circ$ ) from M-ZrPW-0 to M-ZrPW-5, corresponding the d-spacing (100) changed to higher values (from 8.92 nm to 9.49 nm) (shown in Table 1). This indicated that the pore size and unit cell parameter became larger with the introduction of tungsten.<sup>49</sup> The wide angle X-ray diffraction (WXR) patterns of these samples are shown in Fig. 1(2). All the patterns kept consistent with each other and only exhibited two broad peaks in the  $2\theta$  range of  $20-40^\circ$  and  $40-60^\circ$ , indicating the existence of amorphous pore wall structure. No any individual crystalline peaks of zirconium phosphate and zirconia were observed. Meanwhile, there were no peaks of tungsten oxide in the WXR patterns, illustrating the high dispersion  $WO_x$  among the mesoporous framework even in M-ZrPW-20, which had a W/Zr ratio up to 0.2. The same conclusion could also be gotten from the Raman spectra. As shown in Fig. 2, the bulk  $WO_3$  exhibited five bands in the Raman spectra at 815, 725, 332, 280 and  $140\text{ cm}^{-1}$ , which belonged to the crystalline  $WO_3$ . However, there were no obvious bands in these regions in the Raman spectra of M-ZrPW, implying that no crystalline  $WO_3$  existed among the wall of mesostructure. As confirmed by the WXR and Raman spectra characterizations, the tungsten species was highly dispersed among the wall of mesostructure, this might be on account that the W atoms in the materials were segregated by the Zr and P atoms

owing to the peculiar traits of the one-pot preparation strategy.<sup>50</sup> Therefore, the thermal agglomeration of the  $\text{WO}_x$  nanoparticles during the progress of calcination was avoided to some extent, resulting in high dispersion of tungsten species in the mesostructure.

**Figure 1**

**Figure 2**

**Table 1**

In order to further confirm the presence of mesopores in M-ZrPW, TEM (Fig. 3) and SEM (Fig. 4) images of the samples were taken. The TEM images and corresponding FFT patterns revealed the existence of long-range ordered pores along [110] direction (Fig. 3a and c) and [001] direction (Fig. 3b) in the M-ZrPW-0, M-ZrPW-5 and M-ZrPW-10. Further increase the W/Zr ratios to 0.15 and 0.2, M-ZrPW-15 (Fig. 3d) and M-ZrPW-20 (Fig. 3e) showed wormlike mesoporous channels rather than the long-range ordered pores in the TEM images. Although no ordered mesostructure existed in the M-ZrPW-15 and M-ZrPW-20, the abundant wormlike mesopores could be clearly observed in the two samples. The similar feature could also be obtained in the SEM images, which showed ordered mesopores from [110] and [001] directions for M-ZrPW-10 (Fig. 4a and b) and wormlike mesopores for M-ZrPW-20 (Fig. 4c and d). The TEM and SEM images agreed quite well with the results of SXRD characterization, which predicted the presence of ordered mesopores in the samples with W/Zr from 0 to 0.1 and wormlike mesopores

for M-ZrPW-15 and M-ZrPW-20. Furthermore, the corresponding SAED pattern of M-ZrPW-20 was also provided in the inset of Fig. 3e. There were no apparent electron diffraction rings, implying that the wall of the mesoporous framework was amorphous structure, which could also be gotten from the WXR D patterns. In the EDX measurement of M-ZrPW-20 (Fig. 3f), the exclusive peaks of Zr, P and W elements were obviously observed in the pattern, showing that all the elements were successfully introduced into the framework of mesostructure. In addition, the values of W/Zr atomic ratios got from EDX were very close to the theoretical values (shown in Table 2). This might be due to that the tungsten species highly dispersed in the wall of mesopores.

### Figure 3

### Figure 4

The textural properties of the M-ZrPW with different W/Zr ratios were characterized by the N<sub>2</sub>-physisorption. Nitrogen adsorption and desorption isotherms and their pore size distributions (PSD) of the samples are shown in Fig. 5. For all the samples, the isotherms could be classified as type IV with H1 shaped hysteresis loops, which were the typical characteristic of mesoporous materials.<sup>51,52</sup> In addition, all the capillary condensation steps of the hysteresis loops were very steep, indicating the existence of uniform pore size in the framework of M-ZrPW. Meanwhile, as shown in Fig. 5(2), all the PSD were extremely narrow and the position located around 6 nm, once again reflecting the presence of uniform pore size in the mesoporous materials.

Besides, the textural parameters, such as specific surface area, pore size and volume of all the samples were shown in Table 1. With the increasing of W/Zr ratio, the specific surface area ( $\sim 170 \text{ m}^2 \cdot \text{g}^{-1}$ ) and pore volume ( $\sim 0.25 \text{ cm}^3 \cdot \text{g}^{-1}$ ) changed little and the pore size increased slightly from 5.6 nm to 6.5 nm. Although the order degree of mesostructure in M-ZrPW suffered some damage with the W/Zr ratios increased to 0.15 and 0.2, the excellent textural properties were successfully preserved. The introduction of tungsten species had little influence on the textural properties of materials.

### Figure 5

To investigate the calcination process and evaluate the thermal stability of obtained M-ZrPW, TG-DSC analysis profiles of the as-synthesized M-ZrPW-20 in air atmosphere were given in Fig. 6. The TG curve mainly comprised three obvious stages of weight loss during the temperature increase from room temperature to 1000 °C. The first weight loss stage occurred around 150 °C and was designated to the loss of physically absorbed water and other volatile species (like HCl), which were generated in the EISA process. The following sharp weight loss (ca. 45 wt%), along with a drastic exothermic peak in the DSC profile, occurred between at 200 °C and 350 °C, indicating the combustion of the SDAs. The last weight loss lasted from 350 °C to 500 °C was arisen from the further development of the inorganic framework. Besides, no noticeable weight loss was observed over 500 °C, indicating the complete removal of the SDAs. In the DSC profile, there was an exothermic peak at about

800-950 °C and this peak was attributed to the phase transformation of the pore wall. This conclusion could also be further confirmed by the WXR D patterns and Raman spectra of the M-ZrPW-20 calcined at 500-900 °C (shown in Fig. S3).

### Figure 6

### 3.2. Chemical Bonds and Composition Analysis

The UV-vis spectroscopy was employed to characterize the coordination modes and distinguish the tungsten species between incorporated metal and extra-framework metal oxides in M-ZrPW.<sup>53,54</sup> As shown in Fig. 7, the sample without introduction of tungsten (M-ZrPW-0) showed an absorption peak at 205 nm, which was attributed to the Zr-O-P coordination. The weak band at about 300 nm could be due to the interaction of  $Zr^{4+}$  cations with the phosphate counteranions in the mesoporous framework.<sup>55</sup> With the introduction of tungsten, a new broad peak could be observed at about 260 nm. Meanwhile, this peak became more noticeable with the tungsten content increasing from 0.05 to 0.2 and this broad peak should be assigned to the isolated tungsten species or low-condensed oligomeric tungsten oxide species in the wall of mesostructure.<sup>56,57</sup> In addition, the absence of broad peak at about 400 nm, which was attributed to tungsten trioxide and could be observed in bulk  $WO_3$ , might reflect the fact that the tungsten species were highly dispersed in the mesoporous framework and no crystalline  $WO_3$  was formed in M-ZrPW even when the tungsten content reached up to 0.2.<sup>57-59</sup> This conclusion agreed quite well with the results of the WXR D and Raman spectra characterization.

**Figure 7**

The FT-IR spectra of M-ZrPW with different W/Zr ratios were shown in Fig. 8. The M-ZrPW-0 exhibited a broad peak centred at  $1070\text{ cm}^{-1}$ , arising from the Zr-O-P bonds in the mesostructure. Meanwhile, the peaks at  $1630\text{ cm}^{-1}$  and  $3450\text{ cm}^{-1}$  were assigned to the surface hydroxyl groups. Furthermore, with the increasing of tungsten content, a weak peak at  $830\text{ cm}^{-1}$  could be observed and this peak was attributed to the W-O<sub>c</sub>-W vibration in the framework indicating that the tungsten species was successfully introduced into the wall of the mesostructure.<sup>60,61</sup>

**Figure 8**

The high-resolution XPS spectra were employed to investigate the surface chemical composition as well as the oxidation state of tungsten species in M-ZrPW. The W 4f XPS spectra of the M-ZrPW with different W/Zr ratios were shown in Fig. 9. All XPS spectra in the W 4f region were similar to each other in the shape. The core level spectrum displayed two peaks corresponding to W 4f<sub>7/2</sub> and W 4f<sub>5/2</sub> with binding energies of 36.2 and 38.3 eV, respectively. Therefore, it could be inferred that the tungsten species mainly existed as high oxidation state W<sup>6+</sup> in the wall of the mesoporous structure.<sup>62</sup> The high oxidation state W<sup>6+</sup> might account for the improvement of Brønsted acidic property with the increasing of tungsten content in M-ZrPW.



In addition, the surface W/Zr ratios of M-ZrPW were shown in Table 2. These values were determined by the XPS line areas of Zr 3d and W 4f. The W/Zr ratios on the sample surface increased linearly in agreement with the increase of tungsten introduced in the preparation process. Moreover, the W/Zr ratios on the sample surfaces showed only slight differences with the bulk compositions, which calculated from the characterization of XRF. In addition, all the W/Zr ratios gotten from XPS, XRF and EDX characterizations kept consistent with the theoretical values. This indicated that the tungsten species was successfully introduced into the wall and dispersed homogeneously in the wall of mesostructure even when the W/Zr reached to 0.2.

### Figure 9

### Table 2

### 3.3. Acidic Property

The acidic property of calcined M-ZrPW was evaluated by NH<sub>3</sub>-TPD. All the TPD profiles of M-ZrPW-X (shown in Fig. 10(1)) were similar to each other in shape and the characteristic TPD profile showed an obvious broad peak at 150-400 °C and a weak peak at about 600 °C. This indicated that all the samples had abundant acid sites. In addition, the peak strength at 150-400 °C increased from M-ZrPW-0 to M-ZrPW-20, implying that the acidity of M-ZrPW increased with the introduction of tungsten species. This could be further confirmed from the infrared spectra of adsorbed pyridine. The pyridine-IR spectra were employed to evaluate the types and

strength of Brønsted and Lewis acid sites in M-ZrPW with different W/Zr ratios.<sup>46</sup> The pyridine-IR spectra of M-ZrPW-X (shown in Fig. 10(2)) exhibited bands at 1450, 1575 and 1610  $\text{cm}^{-1}$ , demonstrating the existence of Lewis acid sites in the materials. Moreover, the bands at 1540 and 1640  $\text{cm}^{-1}$  were the characteristic bands of pyridinium ion, showing the presence of Brønsted acid sites. In addition, the band at 1490  $\text{cm}^{-1}$  was a combination between two separate bands at 1540 and 1450  $\text{cm}^{-1}$ , corresponding to Brønsted and Lewis acid sites, respectively. These indicated that both Brønsted and Lewis acid sites existed in M-ZrPW. Moreover, it was noteworthy that the bands at 1540 and 1640  $\text{cm}^{-1}$ , which belonged to Brønsted acid sites, were enhanced stepwise with the increase of tungsten content, indicating that the introduction of tungsten species improved the Brønsted acidity of M-ZrPW. In addition, the Brønsted and Lewis acidity gotten from pyridine-IR spectra were shown in Table 3. There were no obvious changes in the Lewis acidity of M-ZrPW, however, the Brønsted acidity increased gradually from 19.9  $\mu\text{mol}\cdot\text{g}^{-1}$  to 55.1  $\mu\text{mol}\cdot\text{g}^{-1}$  with the W/Zr ratios from 0 to 0.2. The improved Brønsted acidity might be due to the highly dispersed tungsten species with high oxidation state ( $\text{W}^{6+}$ ) among the wall of mesostructure, which was introduced through the one-pot EISA strategy. The improved Brønsted acidity might largely influence the catalytic performance of M-ZrPW in the following benzylation reaction.

**Figure 10**

**Table 3**

### 3.4. Catalytic Performance Study

Due to the excellent acidic property, M-ZrPW was used as solid acid catalyst in the liquid phase benzylation of anisole with benzyl alcohol. All the reaction schemes are presented in the Scheme 1.<sup>9,16,63</sup> In this reaction system, benzyanisoles are the products of benzylation of anisole with benzyl alcohol and dibenzyl ether is a product of the auto-etherification of benzyl alcohol. Meanwhile, the dibenzyl ether is also a good benzylating agent, and it can react with anisole to produce benzyanisole.

#### Scheme 1

In the first set of experiments, the benzylation reaction was carried out by using M-ZrPW with different ratios of W/Zr as solid acid catalysts. After reacting at 170 °C for 2 h, *o*-benzyanisole, *p*-benzyanisole and dibenzyl ether were detected as products, whereas *m*-benzyanisole was not detected in the GC instrument. As shown in Fig. 11(1), the variety of tungsten content resulted in a remarkably different reaction activity toward the benzylation reaction. The M-ZrPW-0, without introduction of tungsten, only showed 17.8% conversion of benzyl alcohol. However, with the increase of tungsten content, the conversion increased gradually and reached the maximum conversion 100% for M-ZrPW-20. At the same time, the selectivity of benzyanisole (*o*-benzyanisole and *p*-benzyanisole) for FC benzylation also followed similar regulation. The selectivity observed for M-ZrPW-X gradually increased with the introduction of tungsten species (53.6%, 66.0%, 75.2%, 77.7%, 87.2% for M-ZrPW-X, respectively). It is well known that the benzylation of anisole with benzyl

alcohol is promoted on the Brønsted acid sites.<sup>22,64-66</sup> Therefore, the improvement of catalytic activity might be due to the increase of Brønsted acidic nature which caused by the introduction of tungsten species in M-ZrPW (as shown in Table 3). In addition, a plausible reaction mechanism was presented. As shown in the Scheme 2, the Brønsted acid sites functioned as the catalyst for the formation of benzyl cation ( $\text{C}_6\text{H}_5\text{CH}_2^+$ ) from benzyl alcohol and then  $\text{C}_6\text{H}_5\text{CH}_2^+$  attacked the anisole ring to produce benzyanisole in the course of the FC benzylation.<sup>9,19</sup> In addition, the selectivity of dibenzyl ether, a byproduct of benzyl alcohol, was 46.3%, 34.0%, 24.8%, 22.3%, 12.8% for M-ZrPW-X, respectively. The gradual decrease of dibenzyl ether selectivity kept consistent with the increase of Brønsted acid strength, this might be due to that the dibenzyl ether was used as a benzylating agent and consumed in the benzylation reaction under the existence of sufficient Brønsted acid sites. Due to the better performance of M-ZrPW-20, it was chosen as the representative catalyst for the further studies.

The progress of benzylation of anisole with benzyl alcohol over M-ZrPW-20 was studied by analyzing the reaction product at different time interval (Fig. 11(2)). Initially, the conversion of benzyl alcohol and the yield of benzyanisole were increased with the time and the maximum benzyl alcohol conversion (100%) and benzyanisole yield (87.2%) was achieved at 120 min for M-ZrPW-20. However, the yield of dibenzyl ether increased to the maximum 17.2% only after 60 min, and decreased slightly to 12.8% at 120 min. This might be owing to that the dibenzyl ether was a good benzylating agent, and it was consumed, along with the benzyl alcohol, at

the end of the benzylation reaction. After 120 min, there were little changes in the curves. In addition, the results of leaching test were shown in Fig. 11(2). After removing M-ZrPW-20 from the reaction system at 60 min, there were little changes in the yield of benzyanisole, indicating that the M-ZrPW-20 was truly a heterogeneous catalyst.

### Figure 11

### Scheme 2

Moreover, the effects of catalyst amount on activity were examined and the results were shown in Fig. 12(1). It was found that the conversion and selectivity increased gradually with the amount of catalyst from 0.05 to 0.2 g. The maximum conversion was 100% with 87.2% selectivity when the amount of catalyst reached 0.2 g. The existence of sufficient Brønsted acid sites was beneficial for the improvement of conversion and selectivity. Further increasing the catalyst amount to 0.3 g, the catalytic activity changed little.

The influence of calcination temperature about the activity of M-ZrPW-20 was also investigated. The M-ZrPW-20 treated at 500-900 °C were utilized as catalysts in the benzylation reaction and the results were shown in Fig. 12(2). With the calcination temperature increased from 500 to 700 °C, the conversion and selectivity decreased slightly. This might be due to the decrease of specific surface area with the increase of calcination temperature, just as shown in Table S1. In addition, due to the tungsten species still highly dispersed among the wall of mesostructure (shown in Fig. S3),

there were no drastic declines in catalytic activity. However, there was a drastic decrease of catalytic activity and only showed conversion 50.9% and 13.7% for M-ZrPW-20 treated at 800 °C and 900 °C. As shown in the WXR patterns and Raman spectra of M-ZrPW-20 treated at different temperatures (shown in Fig. S3), the tungsten species in the wall of mesostructure began to aggregate to form crystal  $\text{WO}_3$  and the specific surface area decreased to 45.9 and 10.1  $\text{m}^2\cdot\text{g}^{-1}$  in the M-ZrPW-20 treated at 800 °C and 900 °C. The aggregation of tungsten species and decrease of specific surface area might account for the decrease of catalytic activity after treated at 800 °C and 900 °C. Therefore, we deduced that both the high dispersion of tungsten species and the high specific surface area were in favor of the improvement of catalytic activity.

### Figure 12

In order to check the recyclability of the catalyst, we carried out five runs test over M-ZrPW-20 under the optimized reaction conditions (shown in Fig. 13(1)). Compared with the fresh catalyst, no significant declines in conversion and selectivity were observed after five cycles, indicating that the M-ZrPW-20 could be reused as solid acid catalyst. In addition, the catalyst regenerated after five cycles was characterized by XRD,  $\text{N}_2$ -physisorption and TEM. As shown in Fig. S5 and S6, the mesostructure of M-ZrPW-20 still maintained after five cycles. Meanwhile, the specific surface area, pore size distribution and pore volume changed little, indicating that the catalyst suffered little damage in the acid-catalyzed reaction. Moreover, Fig. 13(2) showed the

activity of M-ZrPW-20 and control catalysts (H-Beta, H-ZSM5 and ZrPW synthesized from the sol-gel method) in the benzylation reaction. Compared with the control catalysts, the M-ZrPW-20 showed a markedly higher catalytic activity. Therefore, the M-ZrPW was a good solid acid catalyst in the benzylation reaction.

### Figure 13

#### 4. Conclusion

A series of M-ZrPW was successfully synthesized through one-pot EISA strategy. The W/Zr ratios of samples could be accurately controlled through dominating the precursors. Meanwhile, the M-ZrPW gotten from this method had obvious mesostructure, large specific surface area, big pore volume and uniform pore size distribution. The tungsten species, introduced through this one-pot strategy, was highly dispersed in the wall of mesostructure. Due to the excellent textural properties and highly dispersed tungsten species, the Brønsted acidic property and reaction activity of M-ZrPW were greatly improved with the introduction of tungsten species. Moreover, the M-ZrPW was successfully used as solid acid catalyst in the liquid phase benzylation of anisole by benzyl alcohol and showed good catalytic performances. Compared with the fresh catalyst, no obvious decrease in catalytic activity was observed after five cycles. Furthermore, the M-ZrPW showed higher catalytic activity than H-Beta, H-ZSM5 and ZrPW synthesized from sol-gel method. Therefore, the M-ZrPW can be employed as solid acid catalyst in the benzylation reaction.

### Acknowledgements

The authors sincerely acknowledge the financial support from the National Basic Research Program of PR China (No. 2011CB201404) and the National Natural Science Foundation of China (No. 21133011).

### Notes and references

<sup>a</sup> State Key Laboratory for Oxo Synthesis and Selective Oxidation, Lanzhou Institute of Chemical Physics, Chinese Academy of Sciences, Lanzhou 730000, People's Republic of China.

<sup>b</sup> University of Chinese Academy of Sciences, Beijing 100049, People's Republic of China.

<sup>c</sup> Suzhou Institute of Nano-Tech and Nano-Bionics, Chinese Academy of Sciences, Suzhou 215123, People's Republic of China.

\* Corresponding author: e-mail: [ljzhou@licp.cas.cn](mailto:ljzhou@licp.cas.cn) (L. J. Chou), Tel: +86 0931 4968066; Fax: +86 0931 4968129

Electronic Supplementary Information (ESI) available: **The SXRD patterns, nitrogen adsorption and desorption isotherms and reaction results of M-ZrPW-25**; the WXR patterns, Raman spectroscopy and nitrogen adsorption and desorption isotherms of M-ZrPW-20 treated at 500-900 °C; XRD patterns, nitrogen adsorption and desorption isotherms and TEM images of the recycled M-ZrPW-20 after five cycles.



1. G. A. Olah, *Friedel-Crafts and Related Reaction*, Wiley-Interscience: New York, 1964.
2. G. A. Olah, *Friedel-Crafts Chemistry*, Wiley, New York, 1973.
3. V.V.Bokade and G.D.Yadav, *J. Nat. Gas Chem.*, 2007, **16**, 186-192.
4. A. Sipos and S. Berényi, *Tetrahedron*, 2008, **64**, 5851-5860.
5. A. Corma and H. García, *Chem. Rev.*, 2003, **103**, 4307-4366.
6. N. Mizuno and M. Misono, *Chem. Rev.*, 1998, **98**, 199-218.
7. J. H. Clark, *Green Chem.*, 1999, **1**, 1-8.
8. K. Tanabe and W. F. Hölderich, *Appl. Catal., A.*, 1999, **181**, 399-434.
9. J. J. Chiu, D. J. Pine, S. T. Bishop and B. F. Chmelka, *J. Catal.*, 2004, **221**, 400-412.
10. C. Tagusagawa, A. Takagaki, S. Hayashi and K. Domen, *J. Am. Chem. Soc.*, 2008, **130**, 7230-7231.
11. K. Okumura, T. Tomiyama, S. Shirakawa, S. Ishida, T. Sanada, M. Arao and M. Niwa, *J. Mater. Chem.*, 2011, **21**, 229-235.
12. A. M. F. Bidart, A. P. S. Borges, L. Nogueira, E. R. Lachter and C. J. A. Mota, *Catal. Lett.*, 2001, **75**, 155-157.
13. N. Narender, K. V. V. K. Mohan, S. J. Kulkarni and I. A. K. Reddy, *Catal. Commun.*, 2006, **7**, 583-588.
14. M. A. Harmer and Q. Sun, *Appl. Catal., A.*, 2001, **221**, 45-62.
15. M. A. Harmer, W. E. Farneth and Q. Sun, *J. Am. Chem. Soc.*, 1996, **118**, 7708-7715.

16. M. H. Al-Hazmi and A. W. Apblett, *Catal. Sci. Technol.*, 2011, **1**, 621-630.
17. M. J. Gracia, E. Losada, R. Luque, J. M. Campelo, D. Luna, J. M. Marinas and A. A. Romero, *Appl. Catal., A*, 2008, **349**, 148-155.
18. M. H. C. de La Cruz, Â. S. Rocha, E. R. Lachter, A. M. S. Forrester, M. C. Reis, R. A. S. San Gil, S. Caldarelli, A. D. Farias and W. A. Gonzalez, *Appl. Catal., A*, 2010, **386**, 60-64.
19. M. H. C. de la Cruz, J. F. C. da Silva and E. R. Lachter, *Catal. Today*, 2006, **118**, 379-384.
20. C. Ramesh Kumar, K. T. V. Rao, P. S. Sai Prasad and N. Lingaiah, *J. Mol. Catal. A: Chem.*, 2011, **337**, 17-24.
21. K.-i. Shimizu, K. Niimi and A. Satsuma, *Appl. Catal., A*, 2008, **349**, 1-5.
22. K. Okumura, K. Yamashita, M. Hirano and M. Niwa, *J. Catal.*, 2005, **234**, 300-307.
23. S. K. Das, M. K. Bhunia, A. K. Sinha and A. Bhaumik, *J. Phys. Chem. C*, 2009, **113**, 8918-8923.
24. J. Dou and H. C. Zeng, *J. Phys. Chem. C*, 2012, **116**, 7767-7775.
25. N. Candu, S. Wuttke, E. Kemnitz, S. M. Coman and V. I. Parvulescu, *Pure Appl. Chem.*, 2012, **84**, 427-437.
26. C. R. Kumar, P. S. S. Prasad and N. Lingaiah, *Appl. Catal., A*, 2010, **384**, 101-106.
27. J. S. Beck, J. C. Vartuli, W. J. Roth, M. E. Leonowicz, C. T. Kresge, K. D. Schmitt, C. T. W. Chu, D. H. Olson and E. W. Sheppard, *J. Am. Chem. Soc.*,

- 1992, **114**, 10834-10843.
28. C. T. Kresge, M. E. Leonowicz, W. J. Roth, J. C. Vartuli and J. S. Beck, *Nature*, 1992, **359**, 710-712.
29. M. Grün, A. A. Kurganov, S. Schacht, F. Schüth and K. K. Unger, *J. Chromatogr. A*, 1996, **740**, 1-9.
30. L. Mercier and T. J. Pinnavaia, *Adv. Mater.*, 1997, **9**, 500-503.
31. N. K. Mal, M. Fujiwara and Y. Tanaka, *Nature*, 2003, **421**, 350-353.
32. Q. Yuan, A. Yin, C. Luo, L. Sun, Y. Zhang, W. Duan, H. Liu and C. Yan, *J. Am. Chem. Soc.*, 2008, **130**, 3465-3472.
33. A. Sinhamahapatra, N. Sutradhar, B. Roy, P. Pal, H. C. Bajaj and A. B. Panda, *Appl. Catal., B.*, 2011, **103**, 378-387.
34. A. Dutta, A. K. Patra, S. Dutta, B. Saha and A. Bhaumik, *J. Mater. Chem.*, 2012, **22**, 14094-14100.
35. K. Nakajima, T. Fukui, H. Kato, M. Kitano, J. N. Kondo, S. Hayashi and M. Hara, *Chem. Mater.*, 2010, **22**, 3332-3339.
36. C. Tagusagawa, A. Takagaki, A. Iguchi, K. Takanabe, J. N. Kondo, K. Ebitani, T. Tatsumi and K. Domen, *Chem. Mater.*, 2010, **22**, 3072-3078.
37. C. Tagusagawa, A. Takagaki, A. Iguchi, K. Takanabe, J. N. Kondo, K. Ebitani, S. Hayashi, T. Tatsumi and K. Domen, *Angew. Chem. Int. Ed.*, 2010, **49**, 1128-1132.
38. C. Tagusagawa, A. Takagaki, A. Iguchi, K. Takanabe, J. N. Kondo, K. Ebitani, T. Tatsumi and K. Domen, *Catal. Today*, 2011, **164**, 358-363.

39. Y. Rao, M. Trudeau and D. Antonelli, *J. Am. Chem. Soc.*, 2006, **128**, 13996-13997.
40. Y. Rao, J. Kang and D. Antonelli, *J. Am. Chem. Soc.*, 2007, **130**, 394-395.
41. J. Kang, Y. Rao, M. Trudeau and D. Antonelli, *Angew. Chem. Int. Ed.*, 2008, **47**, 4896-4899.
42. Z. Miao, L. Xu, H. Song, H. Zhao and L. Chou, *Catal. Sci. Technol.*, 2013, **3**, 1942-1954.
43. J. Fan, S. W. Boettcher and G. D. Stucky, *Chem. Mater.*, 2006, **18**, 6391-6396.
44. Q. Yuan, L. Li, S. Lu, H. Duan, Z. Li, Y. Zhu and C. Yan, *J. Phys. Chem. C*, 2009, **113**, 4117-4124.
45. S. Ghodke and U. Chudasama, *Appl. Catal., A.*, 2013, **453**, 219-226.
46. C. A. Emeis, *J. Catal.*, 1993, **141**, 347-354.
47. P. Yang, D. Zhao, D. I. Margolese, B. F. Chmelka and G. D. Stucky, *Nature*, 1998, **396**, 152-155.
48. D. Zhao, J. Feng, Q. Huo, N. Melosh, G. H. Fredrickson, B. F. Chmelka and G. D. Stucky, *Science*, 1998, **279**, 548-552.
49. W. Cai, J. Yu, C. Anand, A. Vinu and M. Jaroniec, *Chem. Mater.*, 2011, **23**, 1147-1157.
50. L. Xu, H. Song and L. Chou, *Appl. Catal., B.*, 2011, **108-109**, 177-190.
51. K. S. W. Sing, D. H. Everett, R. A. W. Haul, L. Moscou, R. A. Pierotti, J. Rouquerol and T. Siemieniewska, *Pure Appl. Chem.*, 1985, **57**, 603-619.
52. M. Kruk and M. Jaroniec, *Chem. Mater.*, 2001, **13**, 3169-3183.

53. R. S. Weber, *J. Catal.*, 1995, **151**, 470-474.
54. M. S. Morey, J. D. Bryan, S. Schwarz and G. D. Stucky, *Chem. Mater.*, 2000, **12**, 3435-3444.
55. S. K. Das, M. K. Bhunia, A. K. Sinha and A. Bhaumik, *ACS Catal.*, 2011, **1**, 493-501.
56. O. Klepel, W. Böhlmann, E. B. Ivanov, V. Riede and H. Papp, *Micropor. Mesopor. Mater.*, 2004, **76**, 105-112.
57. X. L. Yang, W. L. Dai, R. Gao and K. Fan, *J. Catal.*, 2007, **249**, 278-288.
58. A. Stein, M. Fendorf, T. P. Jarvie, K. T. Mueller, A. J. Benesi and T. E. Mallouk, *Chem. Mater.*, 1995, **7**, 304-313.
59. E. Briot, J.-Y. Piquemal, M. Vennat, J.-M. Bregeault, G. Chottard and J.-M. Manoli, *J. Mater. Chem.*, 2000, **10**, 953-958.
60. B. Orel, U. O. Krašovec, N. Grošelj, M. Kosec, G. Dražič and R. Reisfeld, *J. Sol-gel. Sci. Techn.*, 1999, **14**, 291-308.
61. K. N. Rao, A. Sridhar, A. F. Lee, S. J. Tavener, N. A. Young and K. Wilson, *Green Chem.*, 2006, **8**, 790-797.
62. F. Di Gregorio and V. Keller, *J. Catal.*, 2004, **225**, 45-55.
63. A. B. Deshpande, A. R. Bajpai and S. D. Samant, *Appl. Catal., A.*, 2001, **209**, 229-235.
64. M. H. C. de la Cruz, M. A. Abdel-Rehim, A. S. Rocha, J. F. C. da Silva, A. da Costa Faro Jr and E. R. Lachter, *Catal. Commun.*, 2007, **8**, 1650-1654.
65. T. Kitano, T. Shishido, K. Teramura and T. Tanaka, *J. Phys. Chem. C*, 2012,

**116**, 11615-11625.

66. K. Yamashita, M. Hirano, K. Okumura and M. Niwa, *Catal. Today*, 2006, **118**, 385-391.

**Table 1.** Textural properties of the M-ZrPW-X derived from SXRD and nitrogen adsorption and desorption data

Samples	W/Zr Ratios	SXRD		Nitrogen adsorption and desorption Data		
		$2\theta(^{\circ})$	d-spacing (100) (nm)	Specific Surface Area ( $\text{m}^2\cdot\text{g}^{-1}$ )	Pore Size (nm)	Pore Volume ( $\text{cm}^3\cdot\text{g}^{-1}$ )
M-ZrPW-0	0	0.99	8.92	160.0	5.62	0.22
M-ZrPW-5	0.05	0.93	9.49	161.4	6.54	0.25
M-ZrPW-10	0.10	0.94	9.39	181.5	6.57	0.26
M-ZrPW-15	0.15	0.91	9.70	171.0	6.56	0.24
M-ZrPW-20	0.20	0.94	9.39	168.3	6.26	0.23

**Table 2.** Analysis of the molar ratios of W/Zr in the M-ZrPW-X

Samples	Theoretical values	Calculated from XRF	Calculated from XPS	Calculated from EDX
M-ZrPW-0	0	0	0	0
M-ZrPW-5	0.05	0.04	0.04	0.05
M-ZrPW-10	0.10	0.09	0.08	0.09
M-ZrPW-15	0.15	0.14	0.13	0.15
M-ZrPW-20	0.20	0.18	0.17	0.21



**Table 3.** The acidity of M-ZrPW-X gotten from Pyridine-IR

Samples	Brønsted acidity ( $\mu\text{mol}\cdot\text{g}^{-1}$ )	Lewis acidity ( $\mu\text{mol}\cdot\text{g}^{-1}$ )	Total acidity ( $\mu\text{mol}\cdot\text{g}^{-1}$ )
M-ZrPW-0	19.9	83.0	102.9
M-ZrPW-5	33.2	75.3	108.5
M-ZrPW-10	35.4	81.7	117.1
M-ZrPW-15	38.4	85.8	124.2
M-ZrPW-20	55.1	88.5	143.6

**Figure captions:**

**Figure 1.** Small-angle X-ray diffraction (1) and Wide-angle X-ray diffraction (2) patterns of the M-ZrPW-X: (a) M-ZrPW-0, (b) M-ZrPW-5, (c) M-ZrPW-10, (d) M-ZrPW-15, (e) M-ZrPW-20.

**Figure 2.** Raman spectra of the M-ZrPW-X and bulk  $\text{WO}_3$ : (a) M-ZrPW-0, (b) M-ZrPW-5, (c) M-ZrPW-10, (d) M-ZrPW-15, (e) M-ZrPW-20, (f)  $\text{WO}_3$ .

**Figure 3.** TEM and SAED images of (a) M-ZrPW-0, (b) M-ZrPW-5, (c) M-ZrPW-10, (d) M-ZrPW-15, (e) M-ZrPW-20, (f) EDX measurement of M-ZrPW-20. (The scale in images a-e: 50 nm)

**Figure 4.** SEM images of M-ZrPW-X: (a), (b) M-ZrPW-10 and (c), (d) M-ZrPW-20.

**Figure 5.** Isotherms (1) and pore size distributions (2) of the M-ZrPW-X: (a) M-ZrPW-0, (b) M-ZrPW-5, (c) M-ZrPW-10, (d) M-ZrPW-15, (e) M-ZrPW-20.

**Figure 6.** TG-DSC curves of the as-synthesized M-ZrPW-20.

**Figure 7.** UV-vis diffuse reflectance spectra of the M-ZrPW-X: (a) M-ZrPW-0, (b) M-ZrPW-5, (c) M-ZrPW-10, (d) M-ZrPW-15, (e) M-ZrPW-20.

**Figure 8.** FT-IR spectra of M-ZrPW-X: (a) M-ZrPW-0, (b) M-ZrPW-5, (c) M-ZrPW-10, (d) M-ZrPW-15, (e) M-ZrPW-20.

**Figure 9.** High-resolution XPS spectra of M-ZrPW-X: (a) M-ZrPW-5, (b) M-ZrPW-10, (c) M-ZrPW-15, (d) M-ZrPW-20.

**Figure 10.** (1)  $\text{NH}_3$ -TPD profiles of M-ZrPW-X, (2) IR spectra for pyridine adsorbed on M-ZrPW-X recorded at 150 °C: (a) M-ZrPW-0, (b) M-ZrPW-5, (c) M-ZrPW-10, (d) M-ZrPW-15, (e) M-ZrPW-20.

**Figure 11.** Friedel-Crafts benzylation reaction: **(1)** catalyzed by M-ZrPW-X with different W/Zr ratios; **(2)** catalyzed by M-ZrPW-20 at different times (BA: benzyanisoles, DE: dibenzyl ether).

**Figure 12.** Friedel-Crafts benzylation reaction: **(1)** catalyzed by M-ZrPW-20 with different amount of catalyst; **(2)** catalyzed by M-ZrPW-20 treated at 500-900 °C.

**Figure 13.** Friedel-Crafts benzylation reaction: **(1)** the recyclability of M-ZrPW-20; **(2)** catalyzed by different solid acid catalysts.

**Scheme 1.** Friedel-Crafts benzylation reaction between anisole and benzyl alcohol.

**Scheme 2.** A plausible reaction mechanism of Friedel-Crafts benzylation reaction catalyzed by M-ZrPW-X.

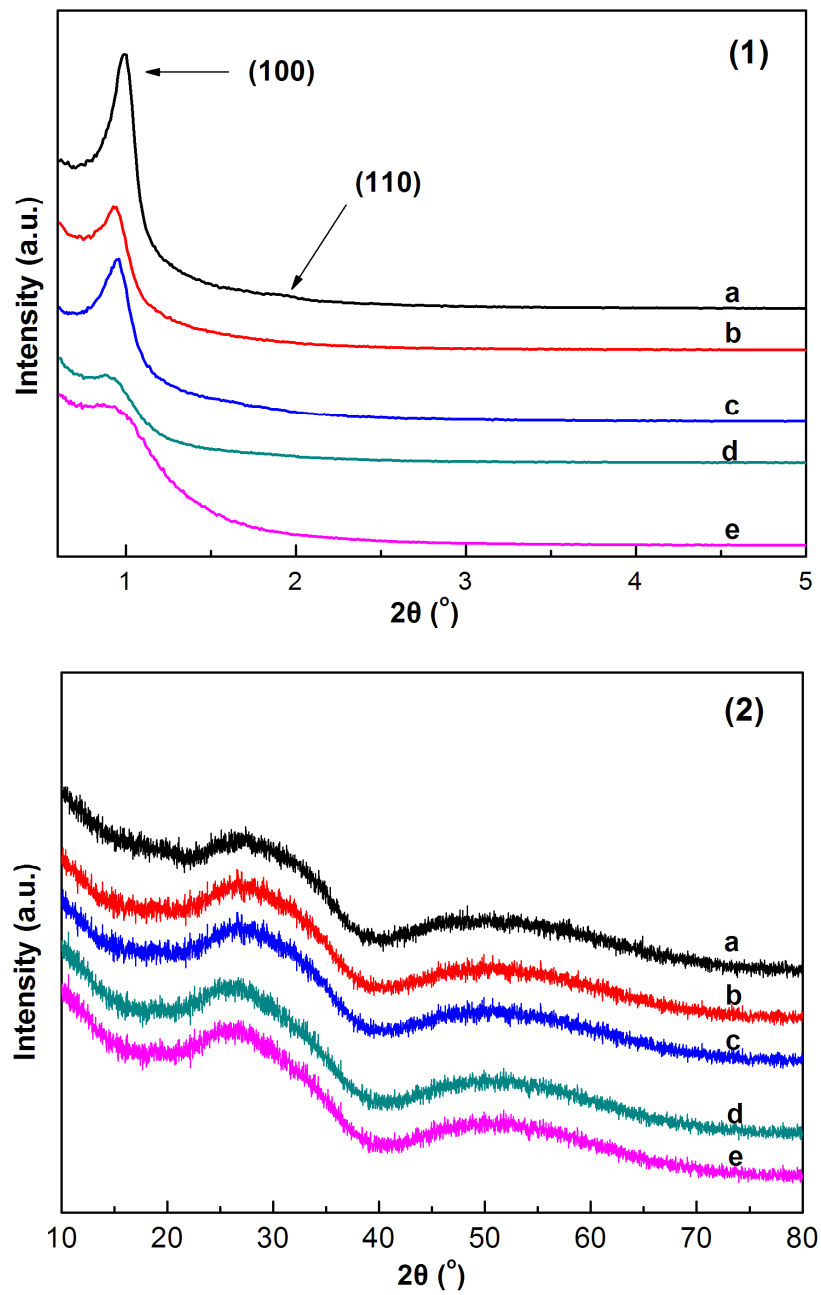


Figure 1

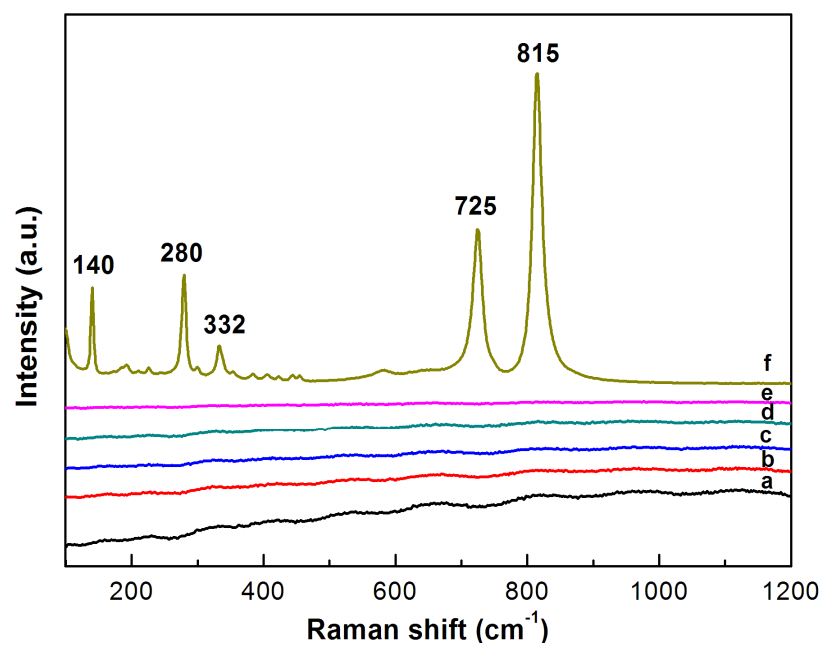


Figure 2

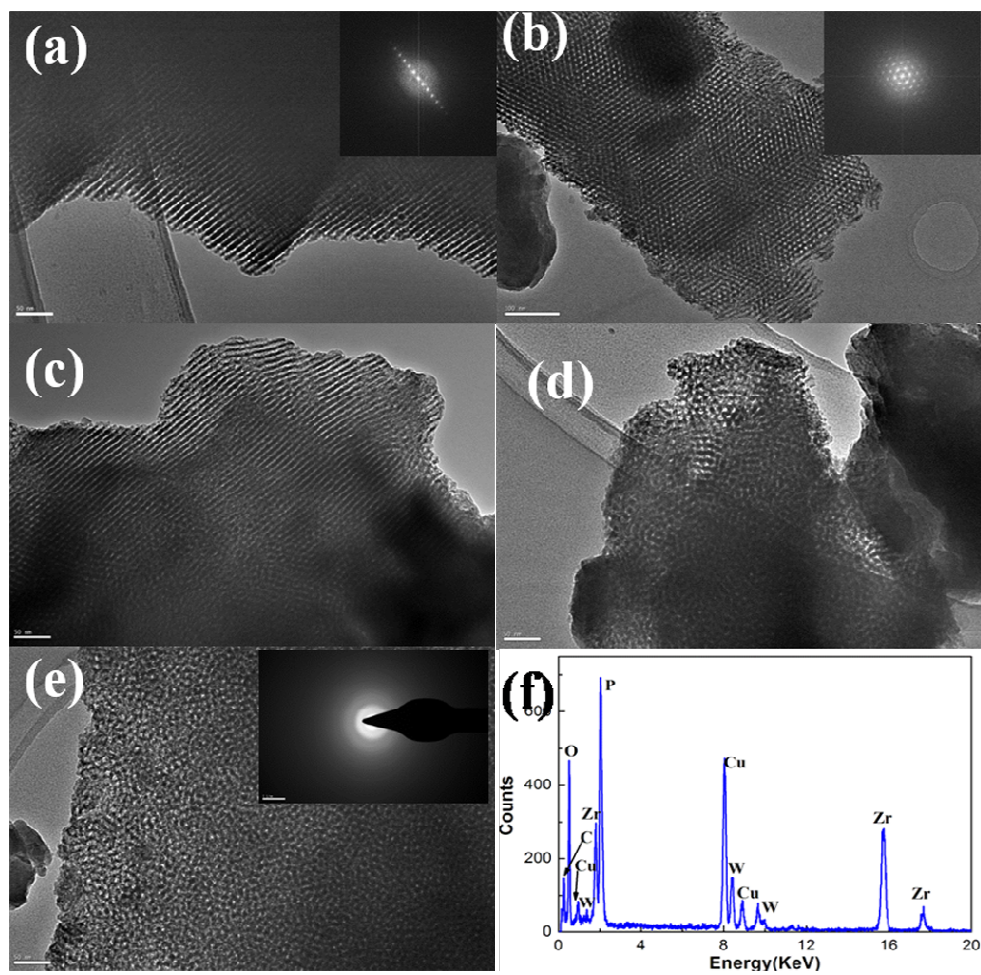


Figure 3

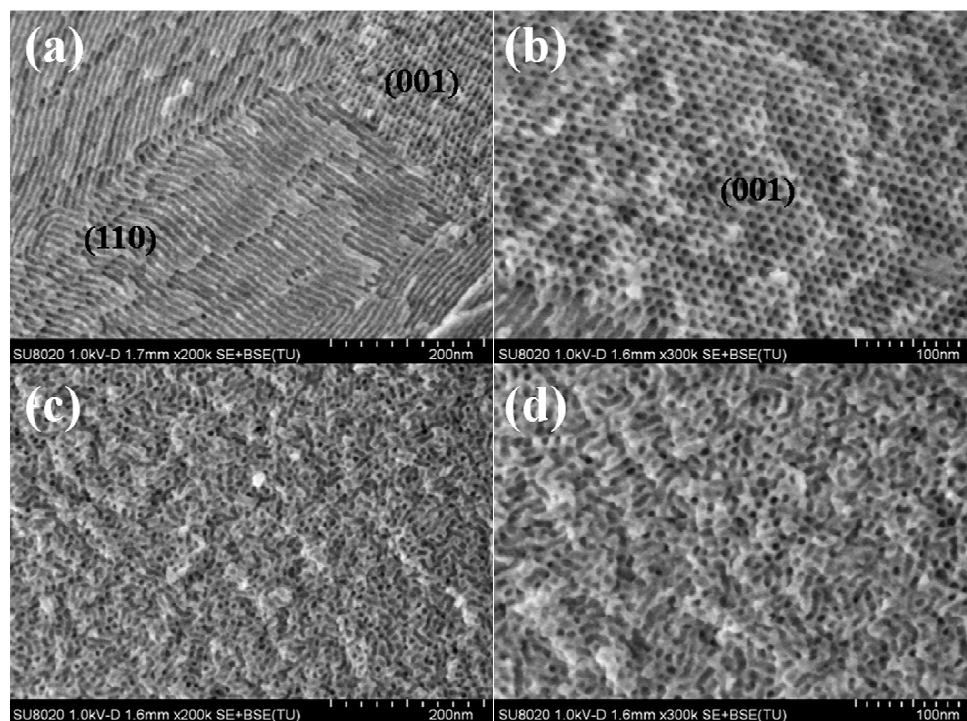


Figure 4

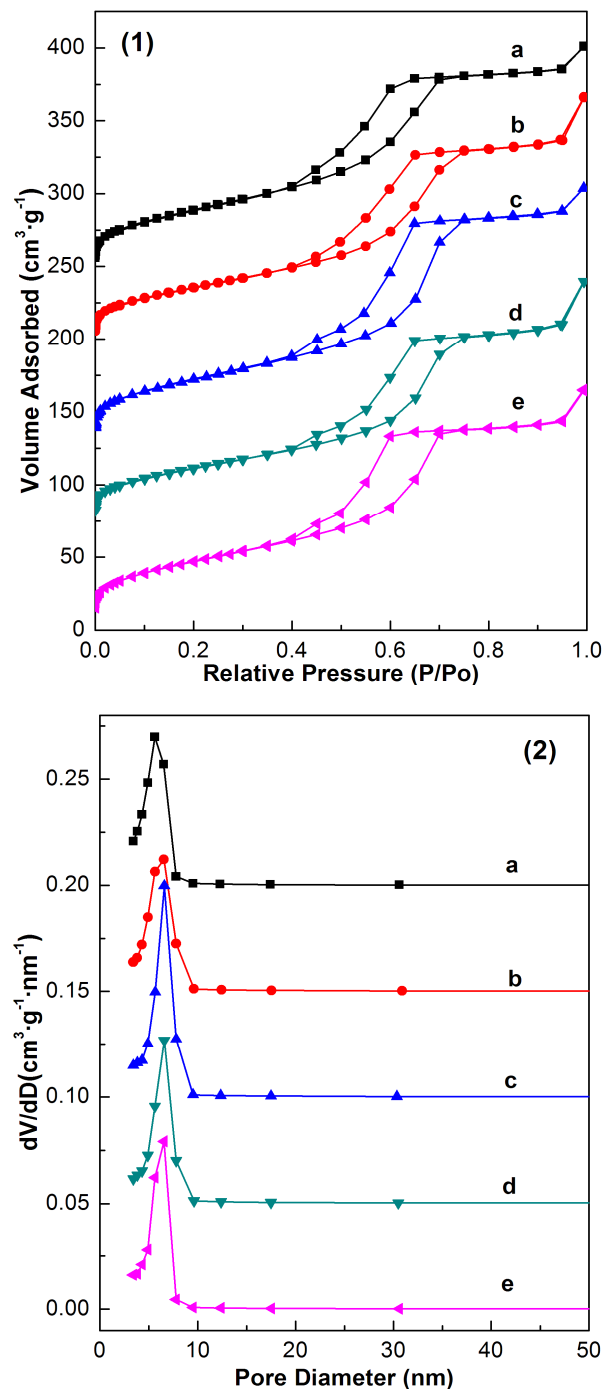


Figure 5



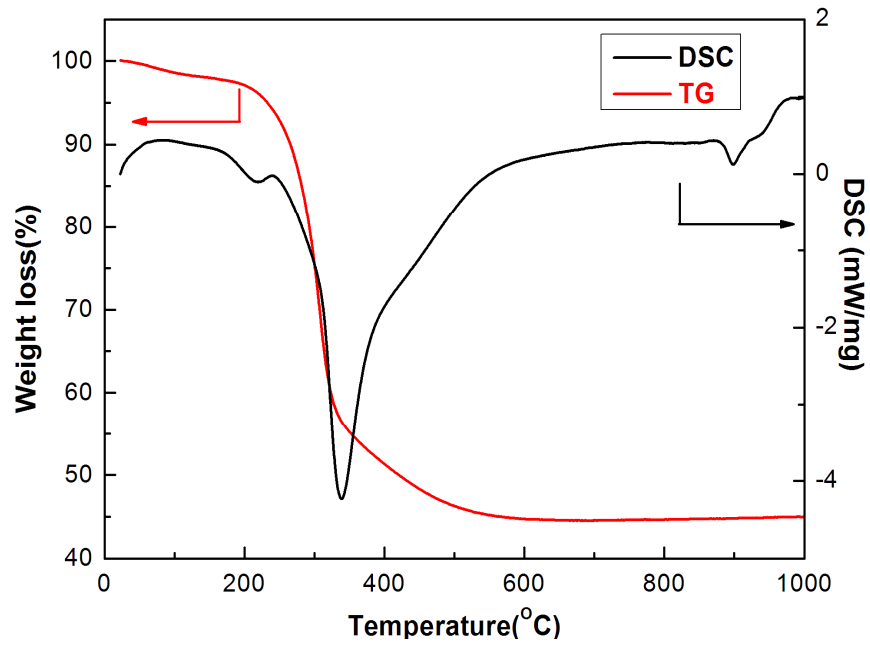


Figure 6

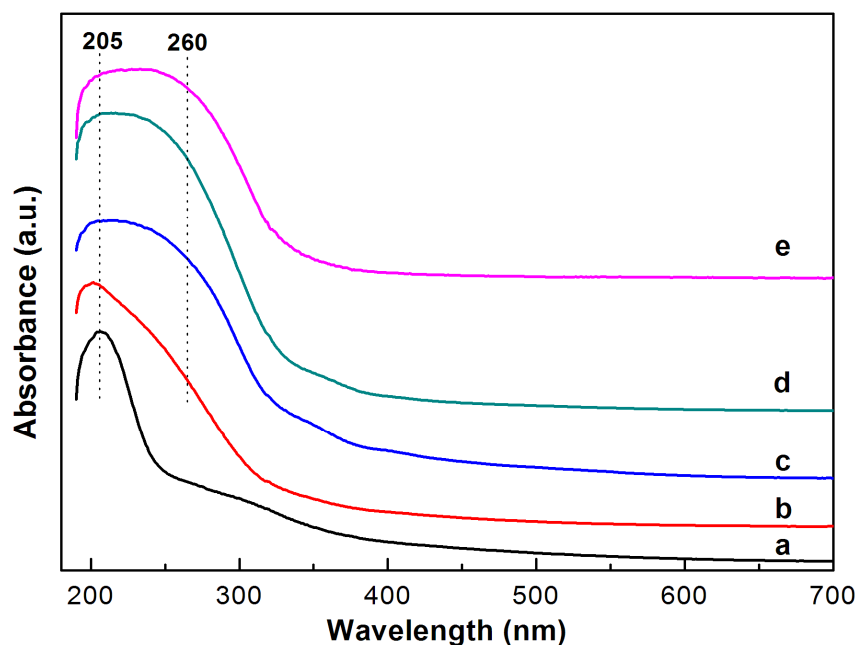


Figure 7

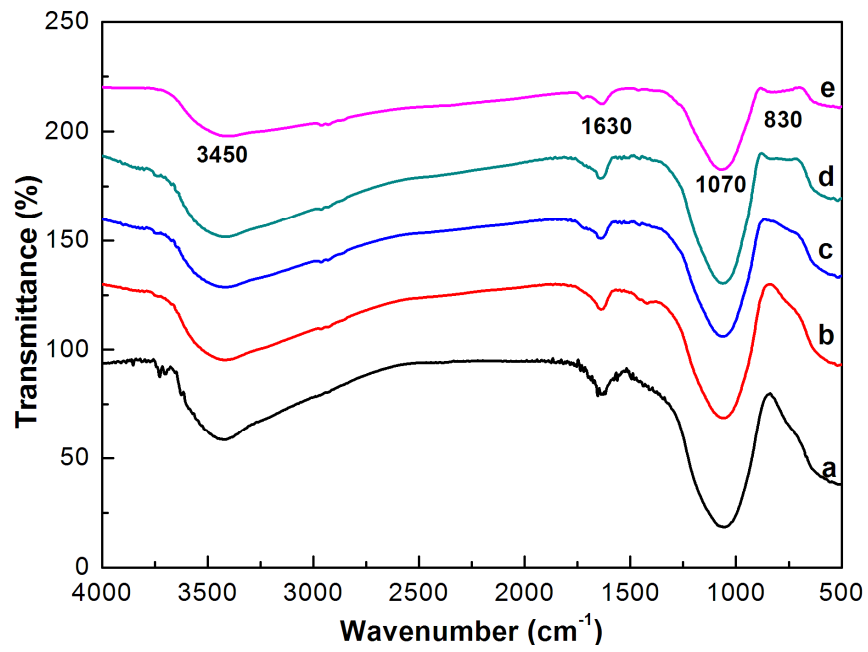


Figure 8

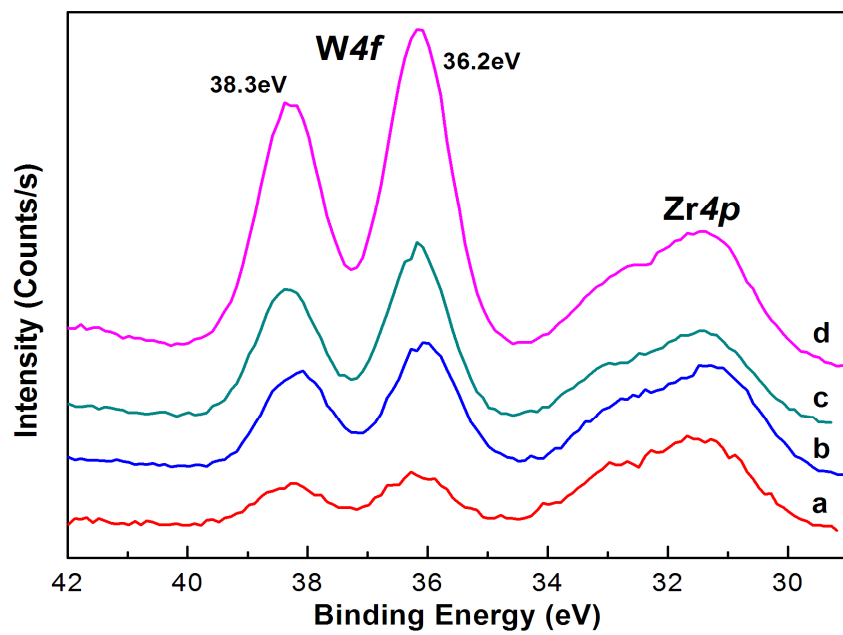


Figure 9

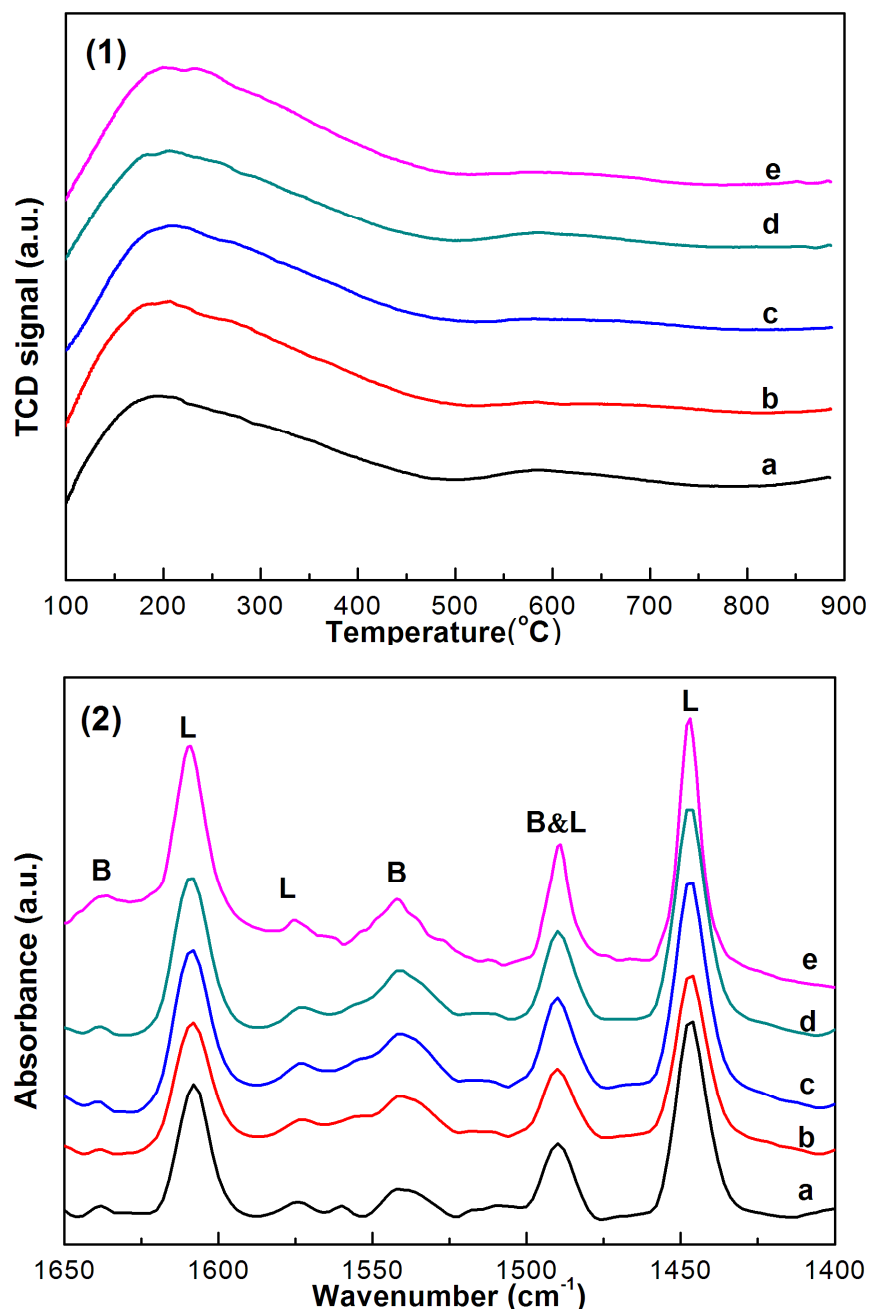


Figure 10

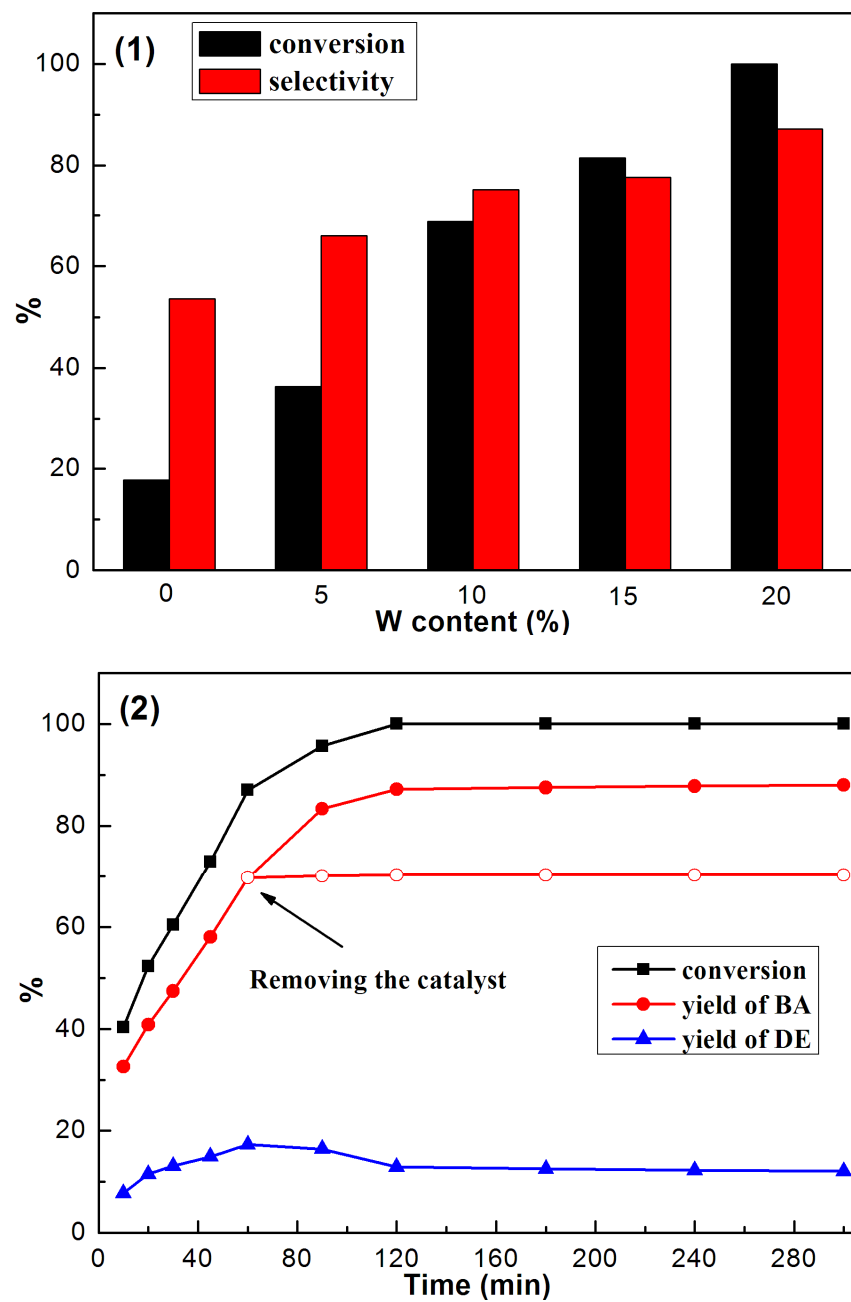


Figure 11

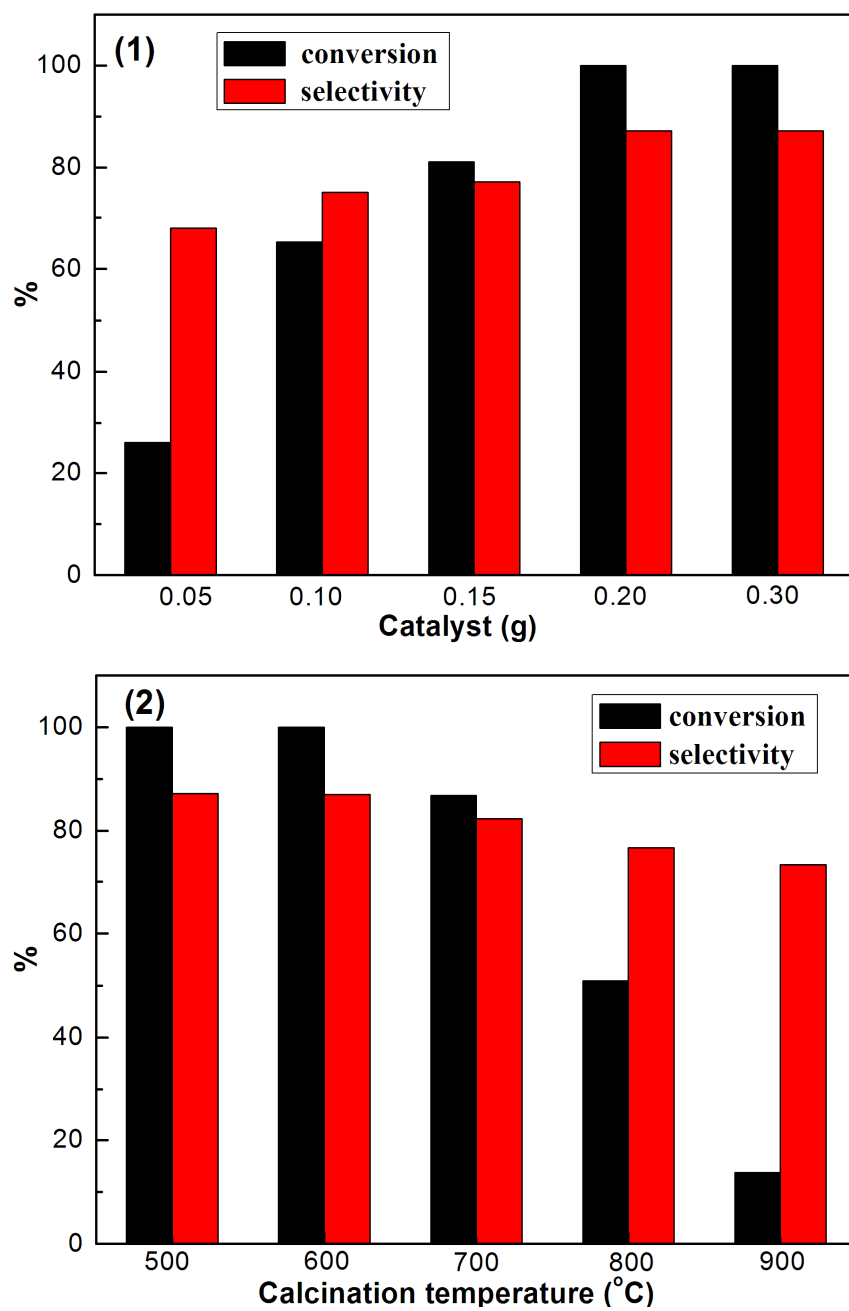


Figure 12

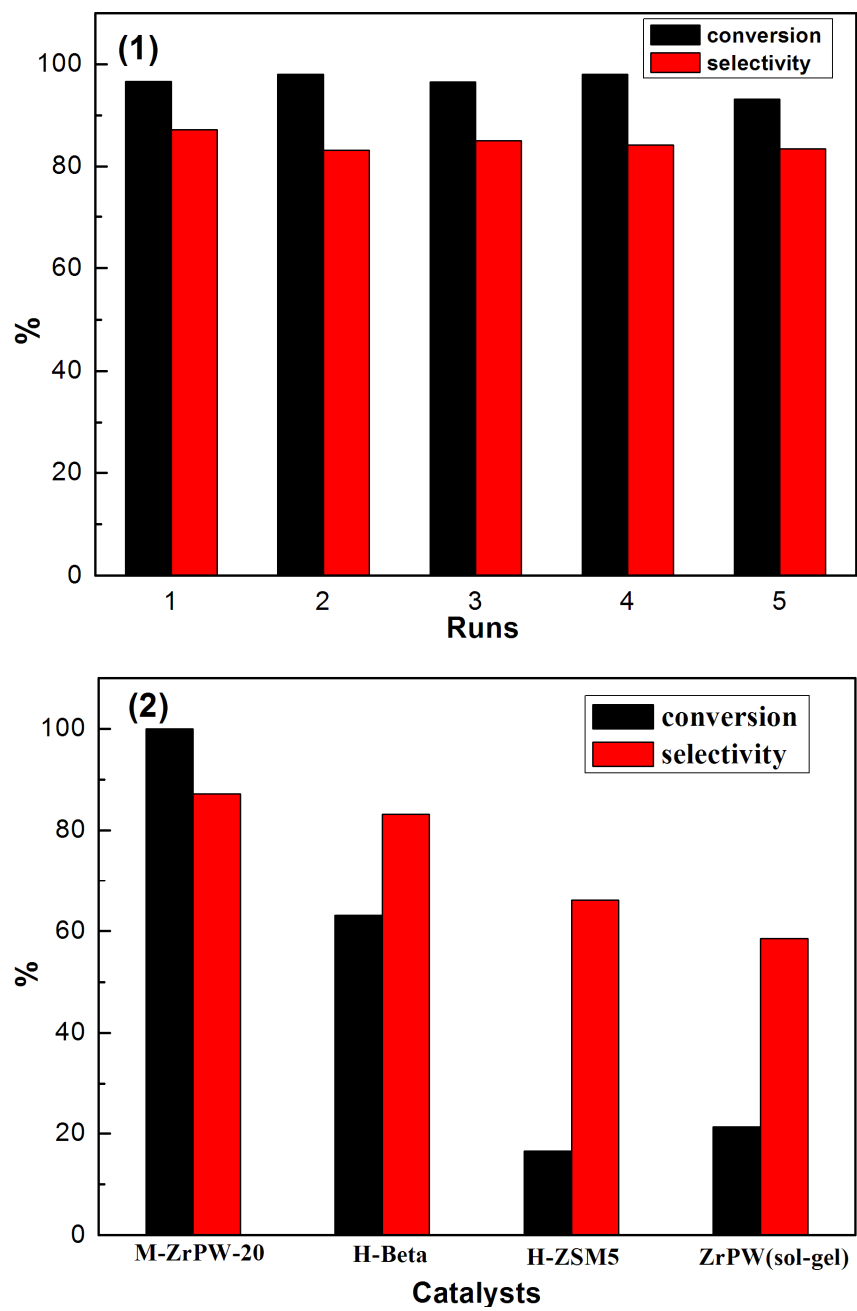
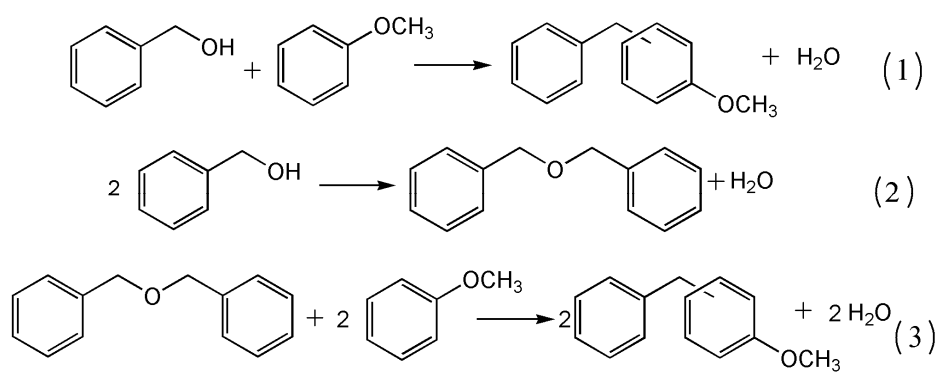
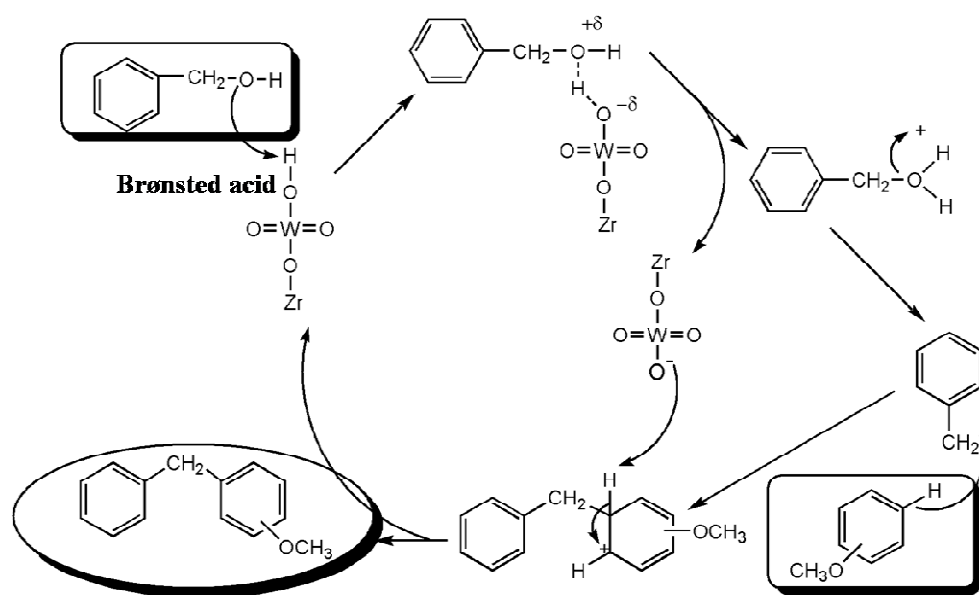


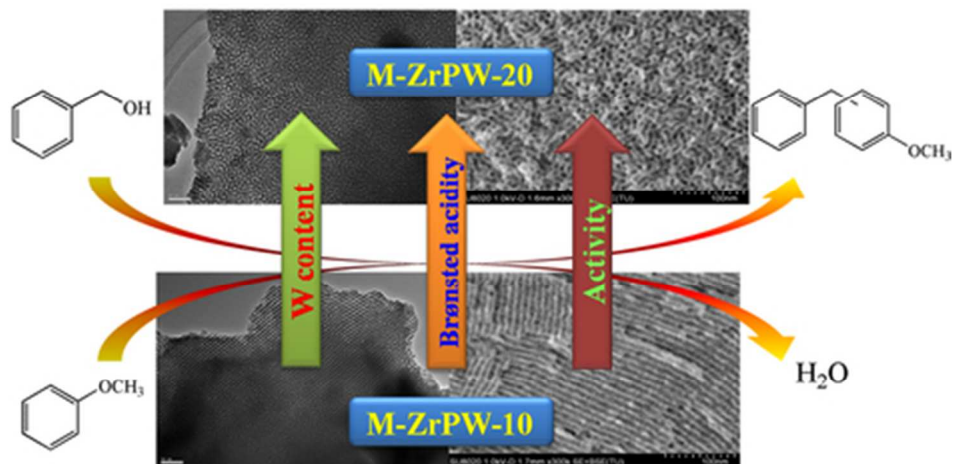
Figure 13





Scheme 1





39x19mm (300 x 300 DPI)